Applied Catalysis B: Environmental 300 (2022) 120728

Contents lists available at ScienceDirect

Applied Catalysis B: Environmental

journal homepage: www.elsevier.com/locate/apcatb

Efficient electrochemical ethanol-to-CO_2 conversion at rhodium and bismuth hydroxide interfaces

Bing Lan [1], Qiong-Lan Wang [1], Zhao-Xia Ma, Ya-Juan Wu, Xiao-Le Jiang, Wei-Shang Jia, Cai-Xia Zhou, Yao-Yue Yang [*,2]

Key Laboratory of General Chemistry of the National Ethnic Affairs Commission, School of Chemistry and Environment, Southwest Minzu University, Chengdu 610041, Sichuan, China

ARTICLE INFO

Keywords:
Rh
Bi
Ethanol oxidation reaction
Alkaline media
CO_2 selectivity

ABSTRACT

Improving the CO_2 selectivity of ethanol oxidation reaction (EOR) is a crucial research topic right now. Rh could effectively break the C—C bond of ethanol, nevertheless, pristine Rh still exhibit negligible EOR activity due to the poisoning effect of C1 intermediates. To solve it, here we fabricate modified Rh interfaces with highly-dispersive $Bi(OH)_3$ species as directed by the Langmuir-Hinshelwood Mechanism, the strong interaction between Rh and $Bi(OH)_3$ could provide the so-called electronic effect and bifunctional effect. Thus it facilitates the C—C bond cleavage at Rh sites and the electrooxidation of as-generated C1 intermediates even at low over-potentials. Eventually, the optimal Rh-$Bi(OH)_3$ catalysts show an apparent C1 pathway faraday efficiency of 26.2% at 0.67 V vs. RHE, the EOR mass activity of ca. 3500 mA $mg^{-1\ Rh}$and 10-hour-long durability. This work could provide an insightful and promising route in promoting the CO_2 selectivity of EOR with high activity and long stability.

1. Introduction

Direct ethanol fuel cells (DEFCs) have been recognized as promising sustainable power conversion devices for portable and mobile applications [1–4]. Nevertheless, the lack of highly efficient anodic electro-catalysts for ethanol oxidation reaction (EOR) has long hindered the further development of DEFCs. It is generally believed that EOR follows a dual-path reaction mechanism [2,5–10], namely the so-called C1 pathway and C2 pathway (see Fig. S1 in Supporting Information). Following the C1 pathway, electrochemical Ethanol-to-CO_2 conversion with 12-electron transferring could obviously benefit the overall power conversion efficiency of DEFCs. Nevertheless, incomplete oxidation of ethanol into acetic acid through the C2 pathway is still predominant in most cases [5–10]. Actually, the most reported platinum-based and palladium-based materials only show a poor C1 pathway selectivity of ca. 1–7.5% at room temperature [7,10–12], even if they significantly improved the reaction rate of ethanol electro-oxidation. Therefore, it's critical and urgent to rationally design and prepare new EOR catalysts with high C1 pathway selectivity.

Recently, researchers found that rhodium (Rh) could be a key component in breaking the C—C bond of ethanol [13,14]. And our previous work [15], employing in situ electrochemical infrared adsorption spectroscopy, indeed demonstrated that ethanol can readily split into C1 intermediates (i.e., CO_{ad} and CH_x species) on Rh surface even at the open circuit conditions. Meanwhile, it also suggested that as-generated C1 intermediates could strongly adsorbed on Rh surface, thus a high over-potential is essential to quickly remove (or oxidize) the C1 intermediates. This could be a convincible explanation to a pretty low mass activity (< 300 mA $mg_{\text{-1Rh}}$) obtained on previously reported Rh-based catalysts, such as cyclic Penta-twinned Rh nanobranches [16], excavated RhNi nanobranches [17], SnO_2-Rh nanosheets [18]. Interestingly, here it becomes to solve a generally known "CO-poisoning effect" on Rh, again, as what we encountered in methanol oxidation on Pt [19], although here CO_{ad} species should be the key active intermediates for EOR C1 pathway rather than the traditional though of poison species [5,7,15]. Note that, it's general thought that CO_{ad} electrooxidation reaction on transition metal surface should follow the so-called Langmuir-Hinshelwood Mechanism [20], where CO_{ad} species and

* Corresponding author.
E-mail address: yaoyueyoung@swun.edu.cn (Y.-Y. Yang).
[1] These authors contributed equally.
[2] ORCID ID: 0000-0002-4573-9437

https://doi.org/10.1016/j.apcatb.2021.120728
Received 4 August 2021; Received in revised form 9 September 2021; Accepted 12 September 2021
Available online 15 September 2021

oxygenated species (OH_{ad} species) first adsorbed on the neighbor sites to form the so-called "reactive pair" of CO_{ad}–OH_{ad} to further lead the generation of CO_2 product. Along this line, the above-mentioned "CO-poisoning effect" on Rh can be effectively solved by introducing the oxyphilic species around the Rh nano-domain, being expected to provide abundant oxygenated species (OH_{ad}) to quickly remove or oxidize the surface adsorbed C1 intermediates. In fact, we recently constructed a Rh-PbO_x catalysts [21] through inhabiting lead and lead oxide around the Rh nano-particles, which displayed superior EOR electro-catalytic performance with the apparent C1 pathway faraday efficiency being as high as ca. 20%. It is understood that here lead oxide should serve as the so-called bi-functional catalysts to enhance the EOR catalysis. Nevertheless, Pb is toxic and could induce great harm to the environment and human health [22], thus it's unsuitable for large-scale practical use. Therefore, it's necessary to found other alternatives with similar oxyphilic characteristics.

Fortunately, bismuth (Bi) takes similar metallic properties with Pb according to the Periodic Law. Actually, Bi and its oxides were considered as the promoter, providing abundant oxygenated species to facilitate the electro-oxidation of small organic molecules on platinum and palladium catalysts [9,23,24]. Specifically, Wang et al. found that the introduction of Bi onto Pt surface significantly inhibited the CO poisoning effect toward formic acid oxidation [25]. Meanwhile, Yuan et al. also developed the PtBi core/Pt shell nanoplates [26], Bi$(OH)_3$/PdBi composite nanochains [27], and porous Pt-Bi$(OH)_3$ catalysts [28] who all displayed efficient methanol and ethanol oxidation performance in alkaline media. Namely, the introduction of Bi to Rh nanoparticles could be a possible strategy to greatly improve the EOR catalysis as that obtained by lead and its oxide in alkaline media.

Thereby, in this work we fabricated the carbon supported Rh-Bi$(OH)_3$ catalysts (named as Rh-Bi$(OH)_3$/C hereafter) by a simple one-pot method, the optimal molar ratio of Rh to Bi is 9/1. The as-prepared catalysts not only effectively break the C—C bond of ethanol and also facilitate the oxidation of C1 intermediates by the abundant OH_{ad} species (confirmed by the in situ electrochemical infrared absorption spectroscopy). Its outstanding EOR activity, durability, and C1-pathway selectivity may provide a possibility to boost the large-scale commercial development of DEFCs.

2. Experimental details

2.1. Materials

Rhodium (III) chloride hydrate ($RhCl_3$, 20765-98-4, $\geq$ 99.95%) was purchased from Shaanxi Kaida Chemical Engineering co., Ltd. Bismuth nitrate ($Bi(NO_3)_3$, 10361-44-1, $\geq$ 99.5%), sodium borohydride ($NaBH_4$, 16940-66-2, $\geq$ 99.7%), ethanol (C_2H_5OH, 64-17-5, $\geq$ 99.7%), and sodium hydroxide (NaOH, 1310-73-2, $\geq$ 99.8%) were purchased from Chengdu Cologne Chemical Co., Ltd. Carbon-supported Pd (Johnson-Matthey, 20 *wt.*% loading), active carbon powder (Vulcan-XC72, Carbot), carbon paper (TORAY TGP-H-060), Nafion solution (Dupont), Nafion 117 membrane (Dupont), deionized water (Milli-Q, 18.25 MΩ cm), high-purity N_2 (99.999%). All chemical reagents were used as received without further purification.

2.2. Synthesis of the catalysts

The Rh-Bi$(OH)_3$/C catalysts were synthesized by $NaBH_4$ reduction method, in a typical synthesis, 3.88 mL 0.05 M $RhCl_3$ aqueous solution and 11 mg $Bi(NO_3)_3$•$5H_2O$ were added into a 100 mL flask and mixed with continuous ultrasonic for 30 min. Then 75 mg pre-activated Vulcan-XC72 carbon powder was put into the flask and magnetically stirred overnight to obtain well-dispersive suspension. Then, 24 mL of 72 mg $NaBH_4$ + 127 mg Na_2CO_3 aqueous solution was pumped (at 0.5 mL min^{-1}) into the suspension in the ice bath, followed by stirring for overnight. Subsequently, the suspension was filtered and washed several times with water and ethanol, and then dried in vacuum at 323 K overnight. For comparison, Rh/C, Bi$(OH)_3$/C catalysts and other Rh-Bi$(OH)_3$/C catalysts with different Rh-to-Bi molar ratio were synthesized similarly expect adding different amount of metal precursors.

2.3. Structural and chemical characterization

The morphology and elemental mapping of as-obtained Rh-Bi$(OH)_3$/C catalysts were characterized by a high-resolution transmission electron microscopy (TEM) (FEI Themis Z operated at 300 KV). The composition of Rh-Bi$(OH)_3$/C were estimated by Energy-Dispersive X-ray Spectroscopy (EDS) equipped in a FEI Quanta 250 FEG Scanning Electron Microscopy (SEM) by box scanning a randomly selected area. The metal loading was roughly analyzed the dissolved aqua regia solution by a SPECTRO ARCOS Inductively Coupled Plasma-Atomic Emission Spectrometry (ICP-AES). The lattice structure of catalysts was measured by X-ray Diffraction Spectrometer (XRD) (BRUKER D8 ADVANCE) with a Cu Kα target, and a Thermo Fisher Kα X-ray Photoelectron Spectroscopy (XPS) were employed to analyze surface valence and electronic structure.

2.4. Electrochemical measurements

The catalyst ink was first prepared by mixing 1 mL of ethanol with water, 2 mg catalyst and 120 μL Nafion. Then pipetting moderate amount of above-mentioned ink upon the polished glassy-carbon electrode surface to serve as the work electrode, keeping the dipped amount of Rh as 28 μg cm^{-2}. Meanwhile a saturated calomel electrode (SCE) and a carbon paper was employed as reference electrode and counter electrode, respectively. In 1 M C_2H_5OH + 1 M NaOH solution, the EOR activity and durability measurement were determined by the cyclic voltammetry and chronoamperometry, respectively. Electrochemical active surface area (*ECSA*) was calculated by the equation of $ECSA = Q/m \cdot C$ [12], where Q is the coulombic charge of the electroreduction of O_{ad} species on catalysts surface, m is the coating mass of catalysts on the glassy carbon electrode, and C is the theoretical amount of charge for reducing the monolayer O_{ad} species (0.405 mC cm^{-2}). The electrochemical impedance spectroscopy (EIS) conducted at the frequency ranging from 1 to 100,000 Hz was employed to evaluate the conductivity and reaction kinetic of catalysts. The potential control and current recording were taken on CHI660E electrochemistry workstation. All the electrolytes were freshly prepared by guarantee reagent (GR) and ultrapure Milli-Q water (18.25 MΩ cm), and all measurements were carried out at room temperature.

2.5. In situ FTIR measurements

The in situ electrochemical attenuated total-reflection (ATR) infrared absorption spectral measurement (see Scheme S1a) was run on a Rh/C and Rh-Bi$(OH)_3$/C catalyst layer covered on an ca. 60 nm thick Au film chemically deposited on the basal plane of a hemicylindrical Si prism using a Agilent Cary 660 FTIR spectrometer equipped with liquid-cooling MCT detector. Then 20 μL above-mentioned catalyst ink was transferred onto an electrochemically polished Au film via a pipette. In this structure, an electrochemical three-electrode system was assembled by using the gold nanometer film as the working electrode (WE) and combining the carbon paper counter electrode (CE) and a saturated calomel electrode (SCE) as the reference electrode (RE). Details of the experiment for the in situ electrochemical infrared reflection absorption spectral (IRAS) measurement (Scheme S1b) can be found elsewhere [7,15,21]. In this work, all spectra are expressed in absorbance units defined as $\log(I/I_0)$, where I and I_0 represent the absorption intensities at the sample and reference conditions, respectively.

2.6. Products analysis and apparent faraday efficiency calculation

Here the EOR products analyses mainly focused on the carbonate (C1 product) and acetate (C2 product). Due to the strong alkalinity of the electrolyte (pH ≈ 14), the amount of bicarbonate in the reaction residual electrolyte could be negligible [12]. To obtain more accurate concentration of products, the EOR should be magnified. In details, the EOR was performed by chronoamperometry for at least 10,000 s in 1 M NaOH + 1 M ethanol solution, controlling the different potential at 0.47, 0.57, and 0.67 V (vs. RHE), respectively. Note that the volume of the electrolyte (*V*) must be accurately controlled. And the total Coulombs (Q_{total}) during the EOR process should be carefully recorded for the following faraday efficiency calculation. The residual solution was pulled out to qualitatively identify the products by Nuclear Magnetic Resonance (NMR) (Agilent, DD2 400-MR). The NMR samples were prepared by dissolving 700 μL residual solution + 35 μL D_2O solution in the NMR tubes [29]. And the quantitative analysis of the concentration of generated acetate (C_{C2}) were carried out by Ionic Chromatography (IC) (Shimadzu, IC-2010 PLUS) rely on a well-documented standard curve, taking the Shodex IC SI-52 4E column and 3.6 mmol Na_2CO_3 solution as the eluent. Thus, the apparent faraday efficiency could be calculated as the equations below.

$$FE_{C2} = \frac{C_{C2} \quad \times V \times 4 \times F}{Q_{total}}$$

$$FE_{C1} = 1 - FE_{C2}$$

where FE_{C2} and FE_{C1} represent the apparent faraday efficiency of EOR C2 pathway and C1 pathway, respectively. *F* is the faraday constant that equals to 96,500 C/mol e, 4 comes from the 4-electron transferring in EOR C2 pathway.

3. Results and discussion

3.1. Structure of catalysts

The morphology of Rh-$Bi(OH)_3$/C sample with Rh-to-Bi molar ratio of 9 (n_{Rh}/n_{Bi} = 9/1) was studied by high-resolution transmission electron microscopy (HR-TEM), and it could be observed that the metal nanoparticles are uniformly distributed on the activated carbon surface (Figs. 1a and S2), with an average diameter of 2.39 ± 0.53 nm. Note that, the bismuth component in Rh-$Bi(OH)_3$/C sample should be in the form of $Bi(OH)_3$ according to the XRD and XPS results below. In the HR-TEM images of Rh-$Bi(OH)_3$/C (Figs. 1b and S2), the lattice space was measured to be ca. 0.22 nm which could be labeled as the (111) plane of Rh [16,30,31]. Nevertheless, it's hard to observe the $Bi(OH)_3$ particles and their corresponding lattice fringes (see the lattice space of $Bi(OH)_3$ in Fig. S3) [32,33], which suggested the high dispersion of $Bi(OH)_3$ clusters with rather small particle size in this Rh-$Bi(OH)_3$/C sample (n_{Rh}/n_{Bi} = 9/1). In contrast, with the amount of $Bi(OH)_3$ increasing, the aggregation and growth of $Bi(OH)_3$ clusters to nanoparticles occurred, which was demonstrated by the particles and lattice fringes of $Bi(OH)_3$ phase in Fig. S3.

To show the distribution of Rh and Bi components, the elemental analysis on a single nanoparticle was carried out by EDS. Fig. 1c show the line-scan EDS results collected on a randomly selected Rh-$Bi(OH)_3$ (n_{Rh}/n_{Bi} = 9/1) nanoparticle, it suggested that Rh and Bi elements were evenly distributed in the nanoparticles. Meanwhile, as shown in Fig. 1d–g, the EDS elemental mapping results on other nanoparticles also visualized that Rh (red) and Bi (green) dots were evenly distributed. Combined with the XRD and XPS results, the structure of Rh-$Bi(OH)_3$ nanoparticles could be determined as the $Bi(OH)_3$ modified Rh nanoparticles (see details below).

XRD and XPS was adopted to further understand the geometric and electronic structure of as-prepared Rh-$Bi(OH)_3$/C catalysts. Specifically, Fig. 2a shows the XRD patterns of as-prepared Rh-$Bi(OH)_3$/C samples,

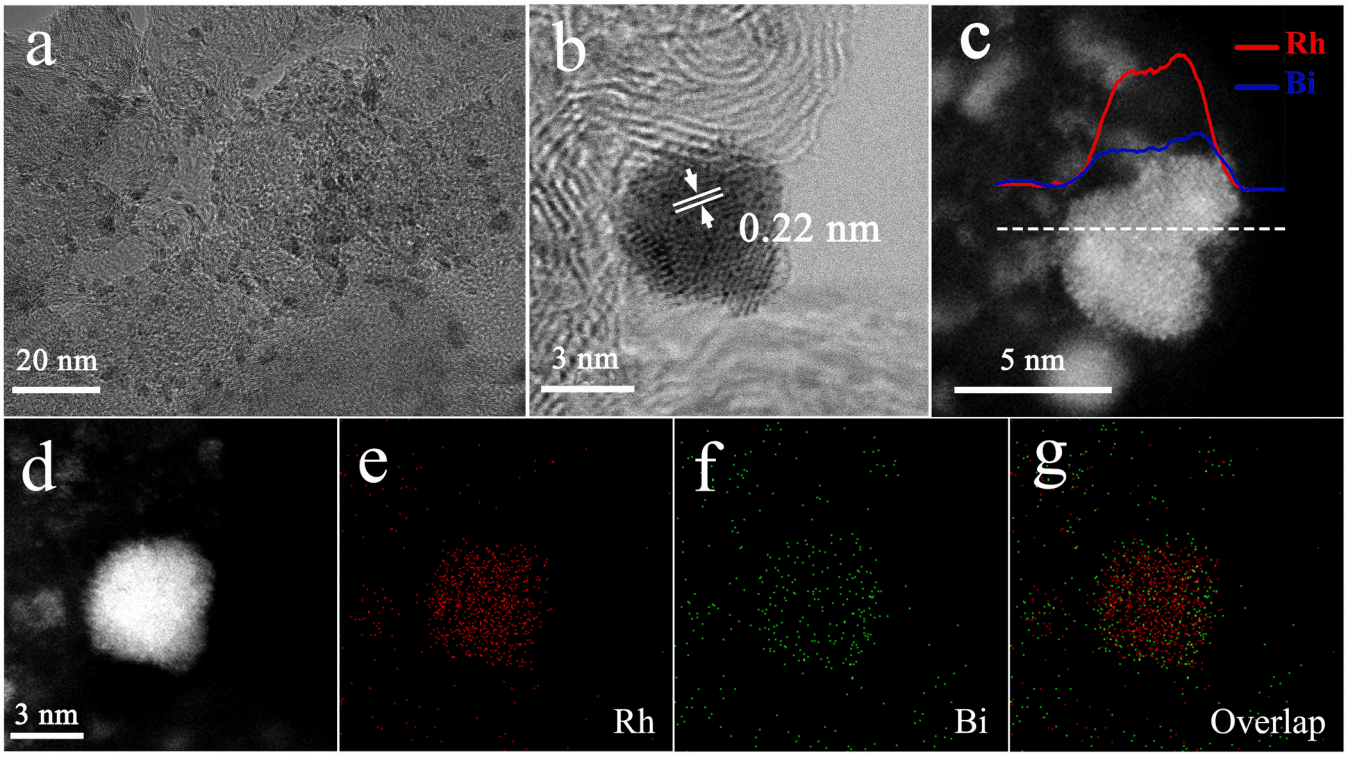

Fig. 1. (a) The typical TEM image and (b) HR-TEM image of Rh-$Bi(OH)_3$/C sample, (c) Corresponding EDS line scan results on a single metal nanoparticle of the Rh-$Bi(OH)_3$/C sample (n_{Rh}/n_{Bi} = 9/1), (d–f) High-angle annular dark field (HAADF) STEM images and elemental mapping analysis of Rh and Bi elements of the Rh-Bi $(OH)_3$/C samples (n_{Rh}/n_{Bi} = 9/1). (For interpretation of the references to colour in this figure, the reader is referred to the web version of this article.)

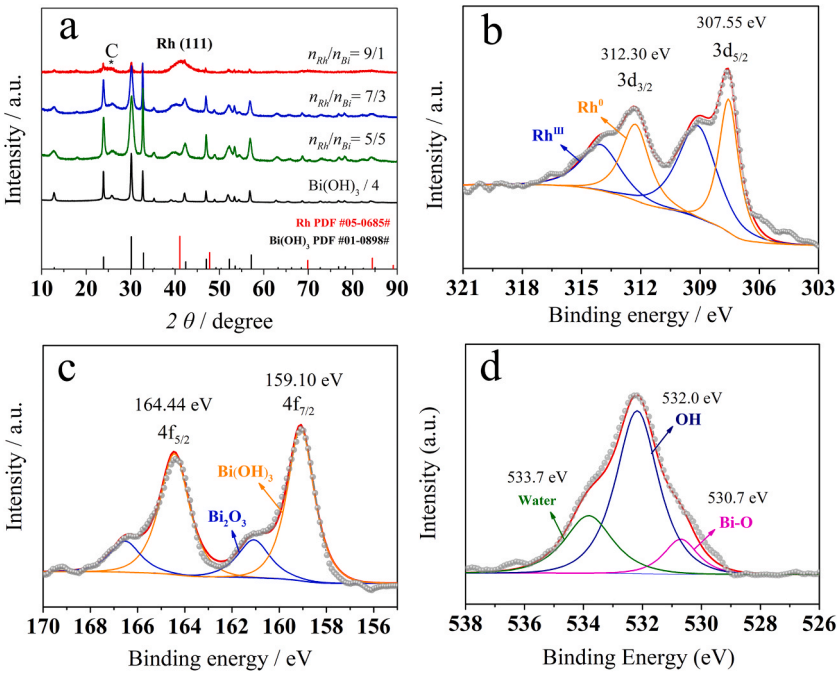

Fig. 2. (a) XRD patterns of the Rh-$Bi(OH)_3$/C (n_{Rh}/n_{Bi} = 9/1, 7/3, 5/5) and $Bi(OH)_3$/C samples, the strength of $Bi(OH)_3$/C samples was compressed by a factor of four. XPS spectra of Rh-$Bi(OH)_3$/C (n_{Rh}/n_{Bi} = 9/1) catalysts for Rh 3d orbital (b), Bi 4f orbital (c) and O 1s orbital (d), respectively.

the diffraction peaks at 41.07°, 47.78°, 69.88°, and 84.39° could be the face-centered cubic (*fcc*) Rh phase (JCPDS card No. 05-0685) [16,17,34], and a series of diffraction peaks also match well with that of the Bi $(OH)_3$ species (JCPDS card No. 01-0898) [32,33]. This result indicated that Rh and $Bi(OH)_3$ phases coexisted in the as-prepared Rh-$Bi(OH)_3$/C samples. And it is interesting that the peak intensity and full width at half max (FWHM) of $Bi(OH)_3$ phase in Rh-$Bi(OH)_3$/C (n_{Rh}/n_{Bi} = 9/1) were pretty smaller than those in Rh-$Bi(OH)_3$/C samples (n_{Rh}/n_{Bi} = 7/3 and 5/5), being indicative of smaller particle size and thus higher dispersion of $Bi(OH)_3$ in Rh-$Bi(OH)_3$/C (n_{Rh}/n_{Bi} = 9/1) than that in Rh-$Bi(OH)_3$/C (n_{Rh}/n_{Bi} = 7/3 and 5/5). Obviously, the higher dispersion of $Bi(OH)_3$ on Rh surface can generate more interfaces between Rh atoms and $Bi(OH)_3$ species. (vide infra).

In addition, none Rh-Bi alloy phase was detected in XRD patterns, which can be supported by the XPS results below. In Fig. 2c, the band at 159.10 and 164.44 eV should be assigned to Bi $4f_{7/2}$ and Bi $4f_{5/2}$ band of $Bi(OH)_3$ species, respectively [26–28]. Besides, the XPS spectra of O 1s further demonstrated the existence of OH species of $Bi(OH)_3$ (532.5 eV), confirming the existence of $Bi(OH)_3$ species in our catalysts. Meanwhile, the bands at 161.08 and 166.6 eV suggests the Bi_2O_3 species were also formed in the catalysts sample [27,35], with the help of detection of Bi—O bond of Bi_2O_3(O1s spectra, 530.9 eV, Fig. 2d) [28]. The Bi_2O_3 species could come from the dehydration of $Bi(OH)_3$ species during the drying treatment in the vacuum oven, considering that no Bi_2O_3 phase was detected in the XRD measurements. In addition, in Fig. 2b, Rh 3d peaks are deconvolved into the doublet, corresponding to the presence of Rh^0 and Rh^{III} species [16]. Note that Rh^{III} species should be due to the exposure of the samples in the air before the ex-situ XPS measurements, which was commonly found before on Pd [36] and Rh surface [21]. It's rather important to find that no Bi^0 species was detected in the Rh-Bi $(OH)_3$/C sample, confirming the above-mentioned conclusion that no detectable Rh-Bi bimetallic alloy formed in our catalysts.

Therefore, based on the above TEM, XRD, and XPS investigation, it could be reasonable to say that the as-obtained Rh-$Bi(OH)_3$/C catalysts should be constituted by the Rh nanoparticles with the surface decoration of $Bi(OH)_3$ species, and the higher dispersion of fine $Bi(OH)_3$ clusters was only obtained in Rh-$Bi(OH)_3$/C (n_{Rh}/n_{Bi} = 9/1) sample, leading to more Rh–$Bi(OH)_3$ interfaces that can enhance the so-called metal-hydroxide-interaction (MOI) effect. The MOI effect is essentially the electronic effect between the metallic Rh and $Bi(OH)_3$ species, which can be proved by the 0.35-eV negative shifting of binding energy of Rh^0 $3d_{5/2}$ band (307.55 eV) in the Rh-$Bi(OH)_3$/C (n_{Rh}/n_{Bi} = 9/1) compared with that of metallic Rh (307.2 eV) [16]. This strong electronic interaction or the MOI effect in the Rh-$Bi(OH)_3$, combined with the so-called bifunctional effect, could beneficially enhance EOR catalysis as described below.

3.2. Electrochemical investigation

The cyclic voltammetric scanning for as-prepared Rh-$Bi(OH)_3$/C (n_{Rh}/n_{Bi} = 9/1), Rh/C and commercial Pd/C were carried out in 1 M NaOH (Fig. 3a). Voltammetric peaks appearing in 0.1–0.3 V were assigned to hydrogen adsorption/desorption on Rh/C and Pd/C catalysts, whereas they almost completely disappeared on Rh-$Bi(OH)_3$/C catalysts. This may be due to weak adsorption of hydrogen species (H_{ad}) due to the abundant surface OH_{ad} species even at the potential region of hydrogen adsorption/desorption (see infrared absorption spectral results below), which is also been found in CO adsorption (theoretically stronger than H_{ad}). As shown in Fig. 3c, different from that on the Rh/C surface, CO adsorption on Rh-$Bi(OH)_3$ surface was basically negligible. And this could be due to the electronic interaction (MOI) between Rh and Bi(OH)3 species as described above, which could upshift the D-band center of Rh to weaken the CO adsorption. Thus we could expect that our Rh-$Bi(OH)_3$ should exhibit an excellent tolerance of CO poisoning and long-term durability for EOR.

In addition, only a very small oxidation peak was found on the Rh/C surface at 0.6 V (Fig. 3a) that is due to the surface adsorption of OH_{ad} species, and its reduction peak was at 0.4 V (Fig. 3a) [37–39]. Meanwhile, the surface oxidation and reduction were at 0.42–0.6 V and 0.2 V on $Bi(OH)_3$/C surface (Fig. S5a), respectively [26,28]. Comparably, Rh-$Bi(OH)_3$/C sample showed an obvious pair of redox peaks with the oxidation and reduction peak at 0.79 and 0.49 V (Fig. 3a), respectively. Apparently, the voltammetric behaviors of Rh-$Bi(OH)_3$/C sample were modulated through the strong interaction of Rh and $Bi(OH)_3$ species, which was also found at the Rh-PbO_x interfaces in our previous work [21] and Rh-SnO_2 interface by Bai et al [18]. Furthermore, the

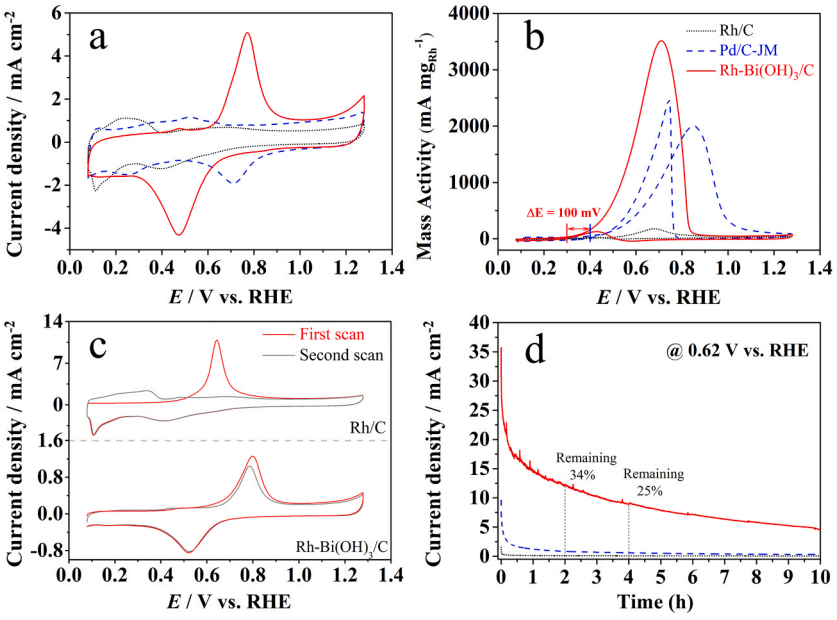

Fig. 3. The CV curves taken on Rh-Bi(OH)$_3$/C (n_{Rh}/n_{Bi} = 9/1), Rh/C, and Pd/C-JM samples in 1 M NaOH solution (a) and 1 M NaOH + 1 M C_2H_5OH solution (b) at 50 mV s^{-1}. (c) the CO monolayer stripping curves collected in 1 M NaOH solution. The CO monolayer was obtained by firstly introducing the CO gas onto surface of Rh/C and Rh-Bi(OH)$_3$/C (n_{Rh}/n_{Bi} = 9/1) samples at ca. 0 V vs. RHE for 20 min and then purging the dissolved CO by high-purity N_2 for at least 1 h under the same potential. (d) The chronoamperometric curves measured at 0.62 V (vs. RHE) with the electrode rotating at 1000 rpm. (a), (b) and (d) share the same legend.

comparative in situ electrochemical infrared absorption spectral results of OH_{ad} adsorption on Rh/C and Rh-Bi(OH)$_3$/C surface, as shown in Fig. S6, clearly show that OH_{ad} formation on Rh-Bi(OH)$_3$/C surface was ca. 300–500 mV lower than that on Rh/C. Thus, as mentioned before, the Rh-Bi(OH)$_3$ interfaces could be more readily to enrich the surface OH_{ad} species even at low over-potentials, being significantly important for the oxidation of C1 intermediates during EOR according to the so-called bifunctional effect (vide infra). On the other hand, the electronic interaction between Rh and Bi(OH)$_3$ species could also weaken the adsorption of C1 intermediates, and thus also facilitate the oxidative remove of surface C1 intermediates.

The EOR catalysis performance of as-prepared samples was evaluated in N_2-saturated 1 M NaOH + 1 M ethanol solution. As shown in Figs. 3b and S5, Rh/C and Bi(OH)$_3$/C samples independently displayed almost no catalytic activity for ethanol oxidation in alkaline media. Whereas, the mass activity of Rh-Bi(OH)$_3$/C (n_{Rh}/n_{Bi} = 9/1) catalyst is as high as 3500 mA mg^{-1} $_{Rh}$(Fig. 3b), nearly twice of that on commonly used commercial Pd/C and 10 times as much as the Pt/C catalysts (Fig. S7). Meanwhile, the onset ethanol oxidation potential on Rh-Bi(OH)$_3$/C (n_{Rh}/n_{Bi} = 9/1) was 100 mV lower than that of the commercial Pd/C-JM catalyst (Fig. 3d). It could be the highest EOR mass activity for Rh-based catalysts as far as our best knowledge (see Table S1). Besides, EOR mass activity was roughly dependent on the Rh-to-Bi molar ratio with the optimized value of 9 (see Fig. S8c) who can merit the high dispersion of Bi(OH)$_3$ species on Rh surface as claimed before. Meanwhile, the EOR stability of the Rh-Bi(OH)$_3$/C samples was measured via chronoamperometry taken at 0.62 V for more than 10 h. In Fig. 3d, the EOR current density on Pd/C and Rh/C was quickly decreasing to zero within 1-hour testing. In contrast, the EOR current density on the Rh-Bi(OH)$_3$/C (n_{Rh}/n_{Bi} = 9/1) was maintained at about 34% and 25% after 2-hour and 4-hour measurement, respectively.

The superior activity and durability could be indirectly understood by the electrochemical active surface areas (*ECSA*) and electro-transfer resistor (R_{ct}) of the electrocatalysts. Actually, *ECSA* was calculated to be 93.22, 65.98, 57.70, 51.70, 45.0 and 14.26 m^2 g^{-1} for Rh-Bi(OH)$_3$/C sample with n_{Rh}/n_{Bi} being equal to 9/1, 8/2, 7/3, 6/4 and 5/5, and the commercial Rh/C, respectively (Fig. S8a-b). Moreover, Electrochemical impedance spectroscopy (EIS) tests show that Rh-Bi(OH)$_3$/C (n_{Rh}/n_{Bi} = 9/1) has the smallest R_{ct} in the Nyquist plots obtained in 1 M NaOH + 1 M C_2H_5OH (Fig. S8d), suggesting that the Rh-Bi(OH)$_3$ interface could also promote the electron transport during EOR [18,40]. In addition, EOR CVs with different scan rates were further employed to investigate the EOR reaction kinetics (Fig. S9a–d). From the linear relationship between peak current during forward scan and the square roots of scan rates (Fig. S9b, d), the EOR kinetics on these catalysts was confirmed to be determined by the diffusion-controlled steps. And the linear slope for Rh-Bi(OH)$_3$/C catalyst (4.16) is much higher than that for the Rh/C catalyst (0.56), indicating more electrons should be involved during EOR under identified conditions [18,40]. Based on the above electrochemical investigation, no wonder that Rh-Bi(OH)$_3$/C (n_{Rh}/n_{Bi} = 9/1) sample show the best EOR activity and durability. Furthermore, the peak current of EOR is highly dependent on the concentration of NaOH (Fig. S9e) and ethanol (Fig. S9f), which is in line with the previous work [40–42].

3.3. CO_2 selectivity of EOR

In Fig. 4a, it is clearly observed that the ν(C-O) band of bridge-adsorbed CO_{ad} species (CO_B) and linearly adsorbed CO_{ad} species (CO_L) at 1758–1842 and 1921–1956 cm^{-1} as EOR ongoing on Rh/C surface, respectively [15,37]. Under the same conditions, the CO spectral band was completely absent on the Rh-Bi(OH)$_3$/C (n_{Rh}/n_{Bi} = 9/1) catalyst (Fig. 4b), indicating that Bi(OH)$_3$ was conducive to promoting the oxidation of CO_{ad} species. Combined with the above-described CO stripping in Fig. 3c, we believed that CO could be more facilely converted to CO_2 on the Rh-Bi(OH)$_3$/C (n_{Rh}/n_{Bi} = 9/1) catalyst.

Besides, IRAS results can effectively detect the products dissolved in the solution in the thin layer. In Fig. 4c, three bands at 1550, 1410, and 1350 cm^{-1} of acetate product (C2 pathway) were detected [11,15–17, 21,28]. A 2341 cm^{-1} band of CO_2 product (C1 pathway) can also be detected at relatively higher potentials [11,15,21,28]. Nevertheless, the carbonate should be the C2 pathway product before CO_2 band emerging. According to our previous study, the asymmetric and symmetric stretching vibration of O-C-O band intensity ratio of neat acetate ($I\nu_{as}$(OCO)/$I\nu_s$(OCO)) should be fixed and averagely equal to ca. 2.6 [21], as shown in Fig. 4d. Whereas, the corresponding ratio obtained on Rh-Bi(OH)$_3$/C (n_{Rh}/n_{Bi} = 9/1) samples is only 1.5. This demonstrated the spectral band of carbonate (1400–1490 cm^{-1}) could be covered in the 1410 cm^{-1} band of acetate [15–17]. Besides, the compositional analysis of reaction residual collected after the electrolysis at a determined constant potential also only detect that acetate and carbonate, employing nuclear magnetic resonance (^{1}H NMR) [29] (Fig. S10) and

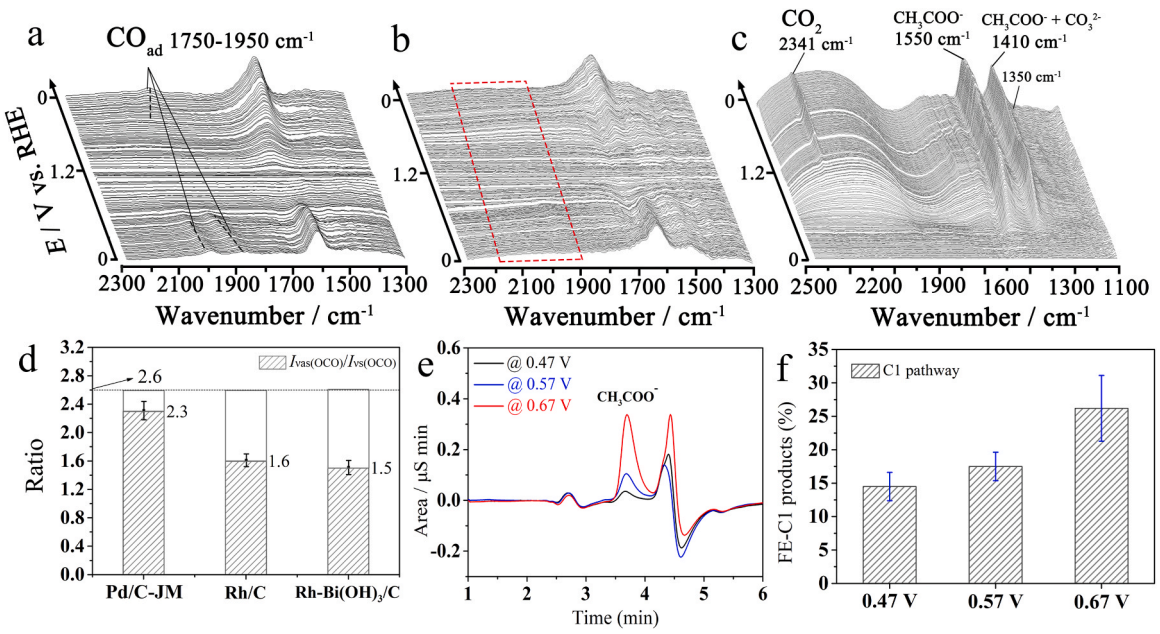

Fig. 4. In situ ATR infrared absorption spectra taken on (a) Rh/C and (b) Rh-Bi(OH)$_3$/C (n_{Rh}/n_{Bi} = 9/1) surface in N_2-saturated 0.1 M NaOH containing 1 M ethanol when the electrode potential scans from 0 to 1.2 V at 5 mV s^{-1}. The Single-beam spectrum at 1.2 V was used as the reference spectrum. (c) In situ IRA spectra collected on Rh-Bi(OH)$_3$/C (n_{Rh}/n_{Bi} = 9/1) catalysts as potential scanning from 0 to 1.2 V at 5 mV s^{-1}, with the reference spectrum obtained at 0 V. (d) The average intensity ratio ($I\nu_{as}$(OCO)/$I\nu_s$(OCO)) of the 1550 cm^{-1} band (ν_{as}(OCO)) to 1410 cm^{-1} band (ν_s(OCO)) taken from the in situ IRA spectra detected on the three catalysts surface as similar to that in Fig. c. (e) Typical IC profiles of the reaction residual on Rh-Bi(OH)$_3$/C (n_{Rh}/n_{Bi} = 9/1) sample with the potential controlled at determined values, where the retention time of acetate is ca. 3.6 min (f) the apparent selectivity of the C1 pathway at different potentials.

ionic chromatography (IC) (Fig. 4e) [12]. Thus, the carbonate should be qualitatively determined as the C1 product for EOR in alkaline media on Rh-Bi(OH)$_3$/C.

To calculate the apparent C1 pathway selectivity, the IC quantitative analysis with a external standard curve method were adopted (see Figs. S11 and 4e-f) to estimate the concentration of produced acetate in the reaction residual. Based on this, we could calculate the consumption amount of the charge according to the well-known Faraday Law as described in the experimental section in Supporting Information. Eventually, the apparent Faraday efficiency of the EOR C1 pathway on Rh-Bi(OH)$_3$/C was about 26.2%, 17.5%, and 14.5% at the working potentials of 0.67, 0.57, and 0.47 V, respectively. The value of ca. 26.2% at 0.67 V is significantly higher than that on Pd/C (ca. 5%, data not shown). And it was visible to the naked eyes that lots of CO_2 bubbles came out on the Rh-Bi(OH)$_3$/C surface while the electrolysis was ongoing at 0.67 V. To be frank, a large error could exist in this calculation method according to our practice, but no better method has been developed so far. We report a conservative value of the C1 pathway selectivity in consideration of the repeatability, even if the values of 50–70% were also obtained several times. Anyway, the above results indicate that the introduction of high-dispersion Bi(OH)$_3$ species onto Rh nanoparticles can effectively improve the EOR selectivity of C1 pathway of Rh-based catalysts.

4. Conclusion

In sum, Rh-Bi(OH)$_3$/C catalysts toward EOR was rationally designed based on the Langmuir-Hinshelwood Mechanism and prepared by a one-pot method. Indeed, as-prepared Rh-Bi(OH)$_3$/C catalysts significantly promoted the EOR catalysis, including mass activity, durability, and especially the CO_2 selectivity. The promotion of EOR catalysis on our catalysts was believed as the following two aspects according to the structure-activity relationship. Initially, based on the TEM, XRD, and XPS investigation, the as-obtained Rh-Bi(OH)$_3$/C catalysts should be constituted by the Rh nanoparticles with the surface decoration of Bi(OH)$_3$ species, leading to abundant Rh–Bi(OH)$_3$ interfaces that trigger the electronic interaction between the metallic Rh and Bi(OH)$_3$ species (MOI effect), which could effectively facilitate the removal of C1 intermediates at lower potentials and thus beneficially enhance EOR catalysis. On the other hand, the Rh-Bi(OH)3 interfaces could be more readily to enrich the surface OH_{ad} species even at low over-potentials, also being significantly important for the oxidation of C1 intermediates according to the so-called bifunctional effect. In a word, at our Rh-Bi(OH)$_3$ catalysts surface, ethanol C—C bond can be split into C1 intermediates at Rh sites, and the as-generated C1 intermediates can be readily oxidative removal due to the strong MOI effect and the bifunctional effect. CO_{ad} species was employed as the model intermediates to confirm this MOI and bifunctional effect. Correspondingly, CO stripping and in situ infrared spectral results show that CO adsorbates almost cannot accumulate on the Rh-Bi(OH)3 surface even at the potential region of hydrogen adsorption, being different from that on Rh surface. Therefore, the Rh-Bi(OH)3/C catalysts showed extremely high mass activity and long-term durability for EOR in alkaline media. More importantly, the apparent faraday efficiency of C1 pathway was estimated as high as 26.2% at 0.67 V vs. RHE. It is expected that this work will provide a beneficial strategy for designing new EOR catalysts with high activity and CO_2 selectivity.

CRediT authorship contribution statement

Bing Lan: Investigation, Writing – original draft preparation. **Qiong-Lan Wang**: Investigation, Writing – review & editing. **Zhao-Xia Ma**: Writing – review & editing. **Ya-Juan Wu**: Writing – review & editing. **Xiao-Le Jiang**: Writing – review & editing. **Wei-Shang Jia:** Writing – review & editing. **Cai-Xia Zhou**: Writing – review & editing. **Yao-Yue Yang**: Conceptualization, Writing – review & editing, Supervision, Project administration, Funding acquisition.

Declaration of Competing Interest

The authors declare that they have no known competing financial interests or personal relationships that could have appeared to influence

the work reported in this paper.

Acknowledgements

This work was supported by NSFC (No. 22172121) and the Fundamental Research Funds for the Central Universities, Southwest Minzu University (xiao2021102).

Appendix A. Supporting information

Supplementary data associated with this article can be found in the online version at doi:10.1016/j.apcatb.2021.120728.

References

[1] Z.W. Seh, J. Kibsgaard, C.F. Dickens, I.B. Chorkendorff, J.K. Norskov, T. F. Jaramillo, Combining theory and experiment in electrocatalysis: insights into materials design, Science 355 (2017), eaad4998.
[2] C. Bianchini, P.K. Shen, Palladium-based electrocatalysts for alcohol oxidation in half cells and in direct alcohol fuel cells, Chem. Rev. 109 (2009) 4183–4206.
[3] A. Rabis, P. Rodriguez, T.J. Schmidt, Electrocatalysis for polymer electrolyte fuel cells: recent achievements and future challenges, ACS Catal. 2 (2012) 864–890.
[4] J. Goldemberg, Ethanol for a sustainable energy future, Science 315 (2007) 808–810.
[5] R. Kavanagh, X.M. Cao, W.F. Lin, C. Hardacre, P. Hu, Origin of low CO_2 selectivity on platinum in the direct ethanol fuel cell, Angew. Chem. Int. Ed. 51 (2012) 1572–1575.
[6] I. Kim, O.H. Han, S.A. Chae, Y. Paik, S.H. Kwon, K.S. Lee, Y.E. Sung, H. Kim, Catalytic reactions in direct ethanol fuel cells, Angew. Chem. Int. Ed. 50 (2011) 2270–2274.
[7] Y.Y. Yang, J. Ren, Q.X. Li, Z.Y. Zhou, S.G. Sun, W.B. Cai, Electrocatalysis of ethanol on a Pd electrode in alkaline media: an in situ attenuated total reflection surface-enhanced infrared absorption spectroscopy study, ACS Catal. 4 (2014) 798–803.
[8] F. Colmati, G. Tremiliosi, E.R. Gonzalez, A. Berna, E. Herrero, J.M. Feliu, The role of the steps in the cleavage of the C-C bond during ethanol oxidation on platinum electrodes, Phys. Chem. Chem. Phys. 11 (2009) 9114–9123.
[9] F.L. Lyu, M.H. Cao, A. Mahsud, Q. Zhang, Interfacial engineering of noble metals for electrocatalytic methanol and ethanol oxidation, J. Mater. Chem. A 8 (2020) 15445–15457.
[10] Y. Wang, S.Z. Zou, W.B. Cai, Recent advances on electro-oxidation of ethanol on Pt- and Pd-based catalysts: from reaction mechanisms to catalytic materials, Catalysts 5 (2015) 1507–1534.
[11] Z.Y. Zhou, Q.A. Wang, J.L. Lin, N. Tian, S.G. Sun, In situ FTIR spectroscopic studies of electrooxidation of ethanol on Pd electrode in alkaline media, Electrochim. Acta 55 (2010) 7995–7999.
[12] W.J. Huang, X.Y. Ma, H. Wang, R.F. Feng, J.G. Zhou, P.N. Duchesne, P. Zhang, F. J. Chen, N. Han, F.P. Zhao, J.H. Zhou, W.B. Cai, Y.G. Li, Promoting effect of Ni $(OH)_2$ on palladium nanocrystals leads to greatly improved operation durability for electrocatalytic ethanol oxidation in alkaline solution, Adv. Mater. 29 (2017), 1703057.
[13] A. Kowal, M. Li, M. Shao, K. Sasaki, M.B. Vukmirovic, J. Zhang, N.S. Marinkovic, P. Liu, A.I. Frenkel, R.R. Adzic, Ternary Pt/Rh/SnO_2 electrocatalysts for oxidizing ethanol to CO_2, Nat. Mater. 8 (2009) 325–330.
[14] M. Li, W.P. Zhou, N.S. Marinkovic, K. Sasaki, R.R. Adzic, The role of rhodium and tin oxide in the platinum-based electrocatalysts for ethanol oxidation to CO_2, Electrochim. Acta 104 (2013) 454–461.
[15] C. Zhu, B. Lan, R.L. Wei, C.N. Wang, Y.Y. Yang, Potential-dependent selectivity of ethanol complete oxidation on Rh electrode in alkaline media: a synergistic study of electrochemical ATR-SEIRAS and IRAS, ACS Catal. 9 (2019) 4046–4053.
[16] J.W. Zhang, J.Y. Ye, Q.Y. Fan, Y.T. Jiang, Y.F. Zhu, H.Q. Li, Z.M. Cao, Q. Kuang, J. Cheng, J. Zheng, Z.X. Xie, Cyclic penta-twinned rhodium nanobranches as superior catalysts for ethanol electro-oxidation, J. Am. Chem. Soc. 140 (2018) 11232–11240.
[17] H.Q. Li, J.Y. Ye, X.M. Li, J.W. Zhang, Y.F. Zhu, Z.Y. Zhou, Y.K. Xue, Y.Q. Jiang, Z. X. Xie, L.S. Zheng, Excavated RhNi alloy nanobranches enable superior CO-tolerance and CO_2 selectivity at low potentials toward ethanol electro-oxidation, J. Mater. Chem. A 7 (2019) 26266–26271.
[18] S.X. Bai, Y. Xu, K.L. Cao, X.Q. Huang, Selective ethanol oxidation reaction at the Rh–SnO_2 interface, Adv. Mater. 33 (2021), 2005767.
[19] N. Kakati, J. Maiti, S.H. Lee, S.H. Jee, B. Viswanathan, Y.S. Yoon, Anode catalysts for direct methanol fuel cells in acidic media: do we have any alternative for Pt or Pt-Ru? Chem. Rev. 114 (2014) 12397–12429.
[20] D.J. Chen, Y.Y.J. Tong, in: K. Wandelt (Ed.), Encyclopedia of Interfacial Chemistry, Elsevier, Oxford, 2018, pp. 881–897.
[21] B. Lan, M. Huang, R.L. Wei, C.N. Wang, Q.L. Wang, Y.Y. Yang, Ethanol electrooxidation on rhodium–lead catalysts in alkaline media: high mass activity, long-term durability, and considerable CO_2 selectivity, Small 16 (2020), 2004380.
[22] B.S. Gillis, Z. Arbieva, I.M. Gavin, Analysis of lead toxicity in human cells, BMC Genom. 13 (2012) 344.
[23] Y.Y. Huang, J.D. Cai, Y.L. Guo, A high-efficiency microwave approach to synthesis of Bi-modified Pt nanoparticle catalysts for ethanol electro-oxidation in alkaline medium, Appl. Catal. B Environ. 129 (2013) 549–555.
[24] A.V. Munde, B.B. Mulik, P.P. Chavan, V.S. Sapner, S.S. Narwade, S.M. Mali, B. R. Sathe, Electrocatalytic ethanol oxidation on cobalt–bismuth nanoparticle-decorated reduced graphene oxide (Co–Bi@rGO): reaction pathway investigation toward direct ethanol fuel cells, J. Phys. Chem. C 125 (2021) 2345–2356.
[25] C.Y. Wang, Z.Y. Yu, G. Li, Q.T. Song, G. Li, C.X. Luo, S.H. Yin, B.A. Lu, C. Xiao, B. B. Xu, Z.Y. Zhou, N. Tian, S.G. Sun, Intermetallic PtBi nanoplates with high catalytic activity towards electro-oxidation of formic acid and glycerol, ChemElectroChem 7 (2020) 239–245.
[26] X.L. Yuan, X.J. Jiang, M.H. Cao, L. Chen, K.Q. Nie, Y. Zhang, Y. Xu, X.H. Sun, Y. G. Li, Q. Zhang, The easier, the better: truth of measurement, Cancer Nurs. 42 (2019) 429–436.
[27] X.L. Yuan, Y. Zhang, M.H. Cao, T. Zhou, X.J. Jiang, J.X. Chen, F.L. Lyu, Y. Xu, J. Luo, Q. Zhang, Y.D. Yin, $Bi(OH)_3$/PdBi composite nanochains as highly active and durable electrocatalysts for ethanol oxidation, Nano Lett. 19 (2019) 4752–4759.
[28] X.L. Yuan, B. Jiang, M.H. Cao, C.Y. Zhang, X.Z. Liu, Q.H. Zhang, F.L. Lyu, L. Gu, Q. Zhang, Novel associations of serum adropin and lipopolysaccharide-binding protein versus lipid profiles in childhood obesity, J. Pediatr. Endocrinol. Metab. JPEM 33 (2020) 265–270.
[29] K.P. Kuhl, E.R. Cave, D.N. Abram, T.F. Jaramillo, New insights into the electrochemical reduction of carbon dioxide on metallic copper surfaces, Energy Environ. Sci. 5 (2012) 7050–7059.
[30] Q. Xue, H. Huang, J.Y. Zhu, Y. Zhao, F.M. Li, P. Chen, Y. Chen, Au@Rh core-shell nanowires for hydrazine electrooxidation, Appl. Catal. B Environ. 278 (2020), 119269.
[31] B.R. Sathe, D.B. Shinde, V.K. Pillai, Preparation and characterization of rhodium nanostructures through the evolution of microgalvanic cells and their enhanced electrocatalytic activity for formaldehyde oxidation, J. Phys. Chem. C 113 (2009) 9616–9622.
[32] K. Bogusz, D. Cardillo, M. Tehei, T. Boutard, P.J. Barker, T. Devers, A. Rosenfeld, S. X. Dou, H.K. Liv, K. Konstantinov, Biocompatible $Bi(OH)_3$ nanoparticles with reduced photocatalytic activity as possible ultraviolet filter in sunscreens, Mater. Res. Bull. 108 (2018) 130–141.
[33] W. Zhang, X.X. Huang, Y.Y. Tan, Y.L. Gao, J.X. Wu, J.B. Hu, A. Stein, B.H.J. Tang, A facile approach to prepare $Bi(OH)_3$ nanoflakes as high-performance pseudocapacitor materials, New J. Chem. 39 (2015) 5927–5930.
[34] B.R. Sathe, B.K. Balan, V.K. Pillai, Enhanced electrocatalytic performance of interconnected Rh nano-chains towards formic acid oxidation, Energy Environ. Sci. 4 (2011) 1029–1036.
[35] B.B. Mulik, B.D. Bankar, A.V. Munde, A.V. Biradar, B.R. Sathe, Bismuth-oxide-decorated graphene oxide hybrids for catalytic and electrocatalytic reduction of CO_2, Chemistry 26 (2020) 8801–8809.
[36] S. Zhang, B. Jiang, K. Jiang, W.B. Cai, Surfactant-free synthesis of carbon-supported palladium nanoparticles and size-dependent hydrogen production from formic acid-formate solution, ACS Appl. Mater. Interfaces 9 (2017) 24678–24687.
[37] C. Zhu, Z.G. Zhao, Y.Y. Yang, Real-time electrochemical ATR-SEIRAS investigation of CO adsorption and oxidation on Rh electrode in 0.1 M NaOH and 0.1 M H_2SO_4, J. Electroanal. Chem. 840 (2019) 462–467.
[38] J.W. Zhang, Y.T. Jiang, S.L. Shi, H.Q. Li, J.Y. Chen, Q. Kuang, Z.X. Xie, L.S. Zheng, Hollow porous rhodium nanoballs, Chem. Commun. 55 (2019) 4989–4992.
[39] Y.Q. Kang, Q. Xue, Y. Zhao, X.F. Li, P.J. Jin, Y. Chen, Cytosolic protein delivery: programed assembly of nucleoprotein nanoparticles using DNA and zinc fingers for targeted protein delivery (Small 52/2018), Small 14 (2018), 1870256.
[40] X.B. Yang, Z.P. Liang, S. Chen, M.J. Ma, Q. Wang, X.L. Tong, Q.H. Zhang, J.Y. Ye, L. Gu, N.J. Yang, A phosphorus-doped Ag@Pd catalyst for enhanced C–C bond cleavage during ethanol electrooxidation, Small 16 (2020), 2004727.
[41] W. Du, K.E. Mackenzie, D.F. Milano, N.A. Deskins, D. Su, X. Teng, Palladium–tin alloyed catalysts for the ethanol oxidation reaction in an alkaline medium, ACS Catal. 2 (2012) 287–297.
[42] Z.X. Liang, T.S. Zhao, J.B. Xu, L.D. Zhu, Mechanism study of the ethanol oxidation reaction on palladium in alkaline media, Electrochim. Acta 54 (2009) 2203–2208.